Eur. Phys. J. E **28**, 113–123 (2009)
DOI 10.1140/epje/i2008-10414-4

THE EUROPEAN PHYSICAL JOURNAL E

Regular Article

Measuring colloidal forces with the magnetic chaining technique

R. Dreyfus[1,a], D. Lacoste[2], J. Bibette[3], and J. Baudry[3]

[1] Center for Soft Matter Research, 4 Washington Place, New York University, New York, 10003 NY, USA
[2] Laboratoire de Physico-Chimie Théorique, ESPCI ParisTech, CNRS UMR 7083, 10 rue Vauquelin, 75005 Paris, France
[3] Laboratoire Colloïdes et Matériaux Divisés, ESPCI ParisTech, UPMC, CNRS UMR 7612, 10 rue Vauquelin, 75005 Paris, France

Received 30 October 2008
Published online: 12 January 2009 –

Abstract. In 1994 Leal Calderon *et al.* (Phys. Rev. Lett. **72**, 2959 (1994)) introduced the magnetic chaining technique to directly probe the force-distance profile between colloidal particles. In this paper, we revisit this approach in two ways. First, we describe a new experimental design which allows us to utilize sample volumes as low as a few microliters, involving femtomoles of surface active macromolecules. Secondly, we extensively describe the characterization and preparation of the magnetic colloids, and we give a quantitative evaluation of performance and resolution of the technique in terms of force and interparticle separation.

PACS. 82.70.Dd Colloids – 47.57.J- Colloidal systems – 87.61.Ff Instrumentation – 81.16.Dn Self-assembly

1 Introduction

Surface forces have been extensively characterized by several techniques. The most common ones are total internal reflection microscopy (TIRM) [1], surface force apparatus (SFA) [2], atomic-force microscopy (AFM) [3], thin-film balance (TFB) [4], and optical or magnetic tweezers (OT or MT) [5–7]. TIRM, SFA, MT and AFM are used to measure forces between two macroscopic surfaces or between a macroscopic surface and a mesoscopic surface, *e.g.* a colloid. OT is a powerful tool for characterizing colloid-colloid interactions, but it is mostly restricted to micrometer scale particles and mainly to long-range interactions.

In this paper, we present a detailed description of another method termed magnetic chaining technique (MCT), which was introduced in 1994 [8]. Similar to OT, MCT was adapted to the measurements of interparticle forces provided that the colloids are magnetic and relatively small, *i.e.* $\approx$ 200 nm in diameter. The experimental setup is remarkably versatile, inexpensive to build, and easy to use. The technique is based on the diffraction of light by chains of magnetic particles responding to an applied magnetic field. It allows the measurement of very small interaction energies per unit area, and interparticle forces as small as 10^{-13} N. Moreover, the force profile measurement is based on averaging over an extremely large number of particles, in contrast to the techniques cited above. MCT has been shown to be very powerful in its ability to measure short-range interactions such as screened electrostatic forces [8], steric forces [9–11], electro-steric forces under polymer-surfactant interaction [12–14] and has been applied more recently to the characterization of small biomolecules such as short DNA [15,16] or proteins [17–19], and to the assembly of magnetic elastic chains [15,18,20]. Primarily, MCT was designed to measure repulsive forces, but it could also be used to measure attractive forces such as depletion forces [21] or the spring constant of extended DNA [15]. This paper is organized as follows: after a presentation of the technique, we describe how to accurately design an apparatus as well as to prepare the magnetic particles. Our contribution concludes with a performance evaluation of MCT.

2 Presentation: principle of the technique

2.1 Interparticle distance measurements and Bragg diffraction

MCT was invented in 1994 by Leal Calderon *et al.* [8], and demonstrated using a monodisperse magnetic emulsion. The emulsion consisted of ferrofluid droplets, obtained using a fractional crystallization technique [22]. The particle radius, a, was approximately 100 nm. These droplets are superparamagnetic: when no magnetic field is applied, the magnetic moments in the iron oxide grains are randomly oriented. Thus, the particles have no global magnetization

[a] e-mail: dreyfus@nyu.edu

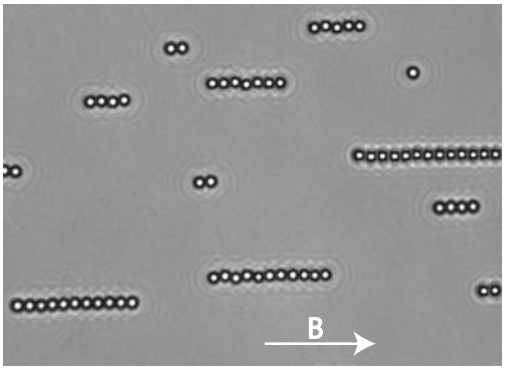

Fig. 1. Videomicroscopy picture of chains of magnetic particles in an external magnetic field ($B = 10\,\mathrm{mT}$). Particles have here a radius a of 525 nm, allowing an easier visualization. Under a magnetic field, magnetic particles get magnetized and align in the direction of the applied field.

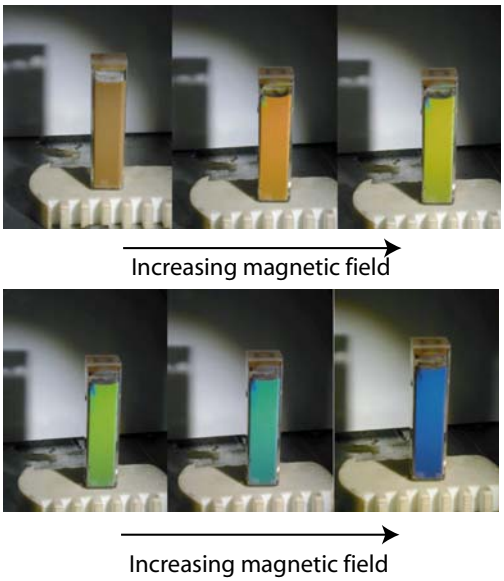

Fig. 2. (Colour online) Change of colors of a solution of magnetic particles. When the magnetic field increases, the interparticle distance decreases, the wavelength diffracted by the chains of particles decreases: the color of the sample changes from red to blue. Ademtech Company.

and they exhibit a Brownian motion. When an external magnetic field is applied, the particles become magnetized and interact, forming chains in the direction of the magnetic field (Fig. 1) in order to minimize their interaction energy. In the presence of the applied field, white-light illumination reveals the sample's beautiful iridescent colors. As the field strength is increased, the sample color changes from red to blue (Fig. 2). This phenomenon can be explained as follows. Because the particle size is of the order of the wavelength of the visible light, and since the particles are monodisperse, each filament suspended in solution forms a lattice that diffracts light in the visible range. The scattered light from each particle in the chain thus interferes constructively as shown in Figure 3. The diffracted wavelength is related to the distance d between the particles in a chain by the well-known Bragg's law:

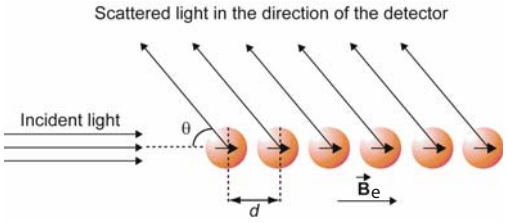

Fig. 3. (Colour online) Light diffracted by a chain of colloids. Each particle scatters the incident light. For a given direction θ, each scattered wave interferes constructively, giving rise to a colored sample.

$$d = \frac{k\lambda}{n(1+\cos(\theta))}\,. \tag{1}$$

Here, k is an integer, λ the wavelength of the incident light in vacuum, n the refractive index of the medium and θ is the angle between the direction of the incident light and the diffracted light as shown in Figure 3. When the applied magnetic field is increased, the attractive magnetic force increases, thereby decreasing the interparticle distance d. According to equation (1), the diffracted wavelength λ must decrease too; thus, the color of the sample changes from red to blue when the magnetic field is increased. The magnetic chaining technique we describe is based on this simple observation.

The interparticle distance d is directly deduced from the measurement of λ with a spectrometer. The distance d results from mechanical equilibrium between the attractive forces and the repulsive forces: the attractive forces include but are not limited to the magnetic dipolar forces $\mathbf{F}^{att}_{mag}$, that depend on d and on the applied magnetic field $\mathbf{B}_e$, and the short-range van der Waals forces $\mathbf{F}^{att}_{vdW}$. The repulsive force $\mathbf{F}^{rep}$ can have various origins; for example it can be electrostatic if the particle surfaces are charged, or steric if a polymer is adsorbed at the surfaces, or both. At mechanical equilibrium:

$$\mathbf{F}^{rep}(d) = \mathbf{F}^{att}_{mag}(d, B_e) + \mathbf{F}^{att}_{vdW}(d). \tag{2}$$

If the amplitude of the magnetic field is increased, the attractive magnetic force increases so that d decreases. By applying equation (2), one can calculate the magnitude of the repulsive colloidal forces $\mathbf{F}^{rep}$ for different values of d and reconstruct the repulsive force profile. In order to perform this calculation, the attractive forces must also be calculated.

2.2 Magnetic interaction within a chain

Knowing the particle separation distance and the external applied magnetic field, the magnetic force is calculated using a model developed by Zhang *et al.* [23]. In this model, a chain of infinite length is considered. The magnetic dipolar force exerted by particle 1 on particle 2 of the same magnetization m is

$$\mathbf{F}_{2\to1} = \frac{3\mu_0 m^2}{2\pi d^4}\mathbf{e}_r\,, \tag{3}$$

where μ_0 is the vacuum magnetic permeability and d is the distance between two particles. Particles form a 1-dimensional infinite crystal of lattice constant d, and the total force exerted by all the beads on a given link in the chain can be calculated as follows. We consider pairs of beads separated by a distance nd, and enclosing a given link in the chain. Each pair exerts on the given link compressive forces given by equation (2) with d replaced by nd. There are n pairs of this kind enclosing a given link, hence the total force is

$$F_{mag}^{att} = \sum_{n=1}^{+\infty} n \frac{3\mu_0 m^2}{2\pi (nd)^4} = \zeta(3) \frac{3\mu_0 m^2}{2\pi d^4}\,, \tag{4}$$

where $\zeta(3)$ is the Riemann zeta-function evaluated at $p = 3$:

$$\zeta(3) = \sum_{n=1}^{+\infty} \frac{1}{n^3} \approx 1.202. \tag{5}$$

Since the attractive force depends on the magnetization of a particle within the chain, the local magnetic field B must be calculated. The field induced by a magnetic particle of magnetization m is

$$\mathbf{B}_{1\to 2}^{dip} = \frac{\mu_0}{4\pi} \frac{2m\cos\theta}{d^3} \mathbf{e}_r + \frac{\mu_0}{4\pi} \frac{m\sin\theta}{d^3} \mathbf{e}_\theta\,. \tag{6}$$

The total local field at the location of particle i is

$$\mathbf{B} = \mathbf{B}_e + \sum_{j\neq i} \mathbf{B}_{dip}^{j\to i} = \mathbf{B}_e + \zeta(3) \frac{\mu_0 m}{\pi d^3} \mathbf{e}_r \tag{7}$$

Indeed, these particles have a very high magnetic susceptibility, so we have to take into account the field-induced by neighboring particles. For paramagnetic materials, the magnetization m depends linearly on the local field $\mathbf{B}$:

$$\mathbf{m} = \frac{4}{3}\chi\pi a^3 \frac{\mathbf{B}}{\mu_0}\,, \tag{8}$$

where χ is the magnetic susceptibility of a particle. The expression of the magnetization is derived by combining equations (7) and (8):

$$m = \frac{4\pi a^3 \chi B_e}{3\mu_0 \left(1 - \frac{\frac{4}{3}\chi\zeta(3)a^3}{d^3}\right)}\,. \tag{9}$$

This calculation shows that the magnetization of a particle inside a chain is 20% higher than that of a single particle in a field B_e. This chaining effect must therefore be taken into account in order to calculate the magnitude F_{mag}^{att} of the attractive force, which is finally given by

$$F_{mag}^{att}(d) = \frac{3\zeta(3)\mu_0 m^2}{2\pi d^4}\,, \quad m = \frac{4\pi a^3 \chi B_e}{3\mu_0 \left(1 - \frac{\frac{4}{3}\chi\zeta(3)a^3}{d^3}\right)}\,. \tag{10}$$

2.3 van der Waals force

The other contribution to the attractive forces is the van der Waals force. Its expression results from the Lifshitz theory [24]. The integrated van der Waals force between two spheres is obtained assuming the Derjaguin approximation ($\frac{d}{a} \ll 1$):

$$F_{vdW}^{att}(d) = \frac{Ha}{12(d-2a)^2} \tag{11}$$

with Hamaker constant H given as

$$H = \frac{3}{4} k_b T \left(\frac{\epsilon_p - \epsilon_w}{\epsilon_p - \epsilon_w}\right)^2 + \frac{3h_p\nu_e}{16\sqrt{2}} \frac{(n_p^2 - n_w^2)^2}{(n_p^2 + n_w^2)^{\frac{3}{2}}}\,, \tag{12}$$

where ϵ_p and ϵ_w are the real part of the dielectric constant of particles and water, n_p and n_w are the refractive indexes of particles and water, h_p is Planck's constant and ν_e is the plasma frequency of an electron gas. The range of van der Walls forces is short enough that we only consider the forces due to the nearest particles. Figure 4 shows the attractive magnetic and van der Waals forces as a function of the surface-to-surface distance h ($h = d - 2a$) between the colloids. Typical values of radius $a = 100\,\text{nm}$, susceptibility $\chi = 1$, and Hamaker constant $H = 10^{-20}\,\text{J}$ are taken in order to calculate the forces. As expected, van der Waals forces are dominant at short distance and become negligible for $h > 20\,\text{nm}$. The magnetic chaining technique is precise enough to measure separation distances as small as 5 nm and for such a range, van der Waals forces cannot be neglected. Therefore, these forces will be taken into account in order to measure the repulsive forces between colloids.

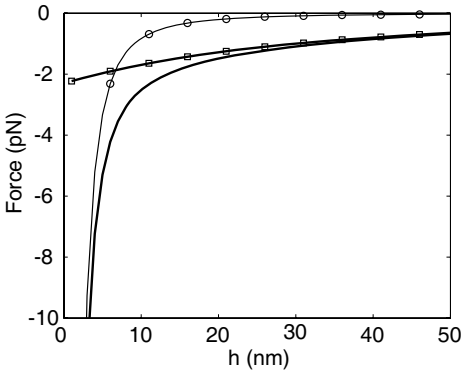

Fig. 4. Attractive forces as a function of the surface-to-suface distance between two colloids. Squares: magnetic force, disks: van der Waals force, solid black line: resultant of the attractive forces.

2.4 Example of electrostatic repulsion

The first experimental measurement of electrostatic interaction between colloidal particles was performed using this technique [8], followed by experiments performed using optical tweezers [5,25]. Here, we present an equivalent measurement performed with our setup. The magnetic particles were washed three times in a 2-(N-morpholino) ethanesulfonic acid buffer (MES buffer), pH = 7, with three different ionic strengths (2 mM, 5 mM, 10 mM) set

by adding sodium chloride (NaCl) to the buffer. The three data sets are shown in Figure 5. At these ionic strengths, the range of the electrostatic forces is short enough that we only consider the forces due to the nearest particles. Therefore, we fitted our data using the law predicted for the electrostatic force profiles assuming a constant potential boundary condition [8]:

$$F_{el} = 2\pi\epsilon\phi_0^2 a\kappa \frac{\exp(-\kappa(d-2a))}{1+\exp(-\kappa(d-2a))}\,, \qquad (13)$$

where ϵ is the dielectric permittivity of the suspending medium, ϕ_0 is the electric surface potential and κ the inverse Debye length. This expression is valid for a thin double layer, *i.e.* $\kappa a \gg 1$, and for particles having a low uniform charge density or low uniform surface potential, $\frac{e\phi_0}{k_B T} \ll 1$, where e is the fundamental charge, k_B the Boltzman constant and T the temperature. Only the surface potential ϕ_0 is used as a fitting parameter. These fits show excellent agreements between the experimental data points and the theoretical predictions. So far we have introduced the technique using previously published models and results. We now present our new apparatus, and describe how to use it. As the technique is based on the use of superparamagnetic particles, we describe in some detail how to adapt and characterize commercial particles, so they can be used for force measurement. Finally we investigate the performance of this new setup, and more generally the validity of the assumptions made for the distance and force calculations.

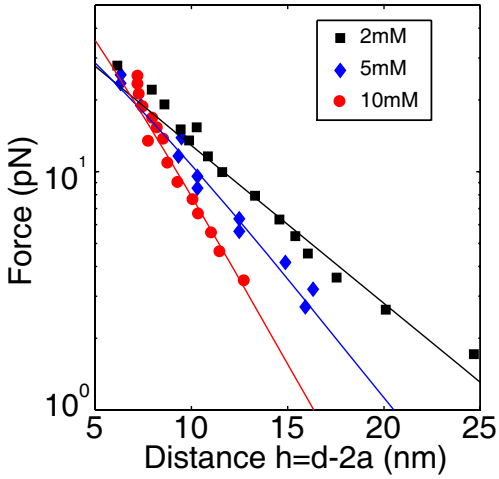

Fig. 5. (Colour online) Measured force-distance profiles of electrostatic forces for three different ionic strengths 2 mM (black squares), 5 mM (blue diamonds), 10 mM (red disks). The solid lines are obtained by fitting the experimental points using equation (13) with the surface potential ϕ_0 as a single adjustable parameter. 2 mM: $\phi_0 = -32$ mV, 5 mM: $\phi_0 = -36$ mV, 10 mM: $\phi_0 = -41$ mV.

3 Design of a new apparatus

3.1 Experimental setup

The different parts of the setup are presented in Figure 6. Our main motivation was to reduce the amount of particles needed for a measurement, which is important for application to biological objects. In addition, we wanted to improve the resolution in distance measurements, and to characterize this resolution. Each experimental component was chosen with these constraints in mind. The sample cells we use are made of two square pieces of glass separated by two nylon wires of 100 μm in diameter. Such cells allow us to use a very small volume of liquid containing particles (40 μL). They are especially designed so that they are sufficiently large to be exposed to the whole incident light. Since the colloids are aligned in a magnetic field, it is important to design a coil that generates a sufficiently high magnetic field, and such that the diameter of the coil is large enough to impose a homogeneous magnetic field on the sample. For that purpose the following coil was designed: the internal diameter is 9 cm and the outer diameter is 28 cm. The coil is 11.6 cm in width. The copper wire has a 2 mm diameter, its length is 1000 m. The coil is cooled with a water circulation bath, its electrical resistance is 5.4 Ω. The magnetic field is directly proportional to the current flowing inside the coil, the maximum intensity and voltage the generator is able to deliver are

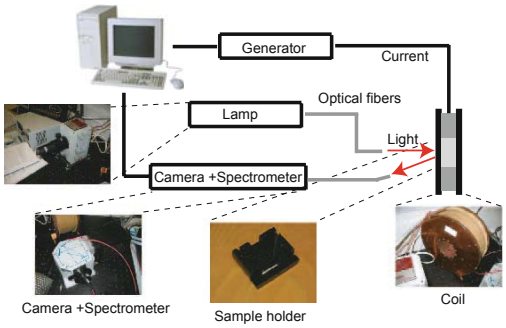

Fig. 6. Scheme of the experimental setup. The generator and the camera are computer controlled. The light is emitted and collected through optical fibers.

18 A and 60 V. A special sample holder is designed to fit inside the coil. With such a coil, the magnetic field can vary between 0 and 100 mT which is the range of interest for our experiments. The illumination of the sample is due to a 75 W xenon vapor lamp of power (Oriel). The light is guided through a bundle of optical fibers, with a diameter of 1.6 mm and an acceptance cone of 31°. The end of the fiber is located at the focal point of a lens (focal $f = 19$ mm, diameter $d = 11$ mm). The light emerging from the lens is parallel and illuminates the sample located at 12 cm. The setup is designed such that the incident light is perpendicular to the sample inside the coil. The scattered light is collected into a second fiber of diameter $d = 0.6$ mm and acceptance cone 22°, located at the focal point of a convergent lens ($d = 11$ mm, $f = 19$ mm) located at 14.4 cm from the sample. The fiber passes into a spectrometer in which an optical grating of 400 lines/mm of blaze wavelength 500 nm is located. The different wavelengths of the light are reflected, separated and sent to a

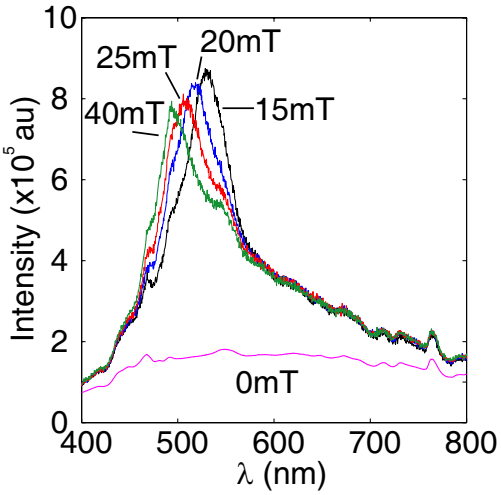

Fig. 7. (Colour online) Spectra of light scattered by magnetic particles under magnetic fields of different intensities, 0 mT (purple), 15 mT (black), 20 mT (blue), 25 mT (red) and 40 mT (green). A clear shift towards lower wavelength is observed due to the decreasing interparticle distance.

Ropper Scientific Back Illuminated Camera whose CCD contains 1340×100 pixels. The CCD pixels are sensitive in the visible spectrum, between 350 and 800 nm. This feature of the CCD actually determines the choice of the angle between the emitting fiber and the collecting fiber. Indeed, for particles of 180 nm in diameter, according to equation (1), the diffracted wavelength is located in the visible spectrum only if $60° > \theta > 0°$. Moreover, the uncertainty Δd on the measurement of the distance is related to the uncertainty $\Delta\lambda$ through $\Delta d = \frac{\Delta\lambda}{n(1+\cos(\theta))}$. To reduce this cause of uncertainty as much as possible, it is better to set a configuration where θ is as small as possible. It is also important to have θ high enough not to collect the light that is directly reflected on the glass of the sample. That is the reason why we choose $\theta = 17°$. The entire setup is computer controlled. The current generator and the camera are controlled using Labview software.

3.2 Analysis of the spectrum of the scattered light intensity

Typical measured signals are shown in Figure 7 for a volume fraction $\phi_v = 3 \cdot 10^{-3}\%$, corresponding to a bead concentration of $C = 16 \cdot 10^{-12}$ mol/L. The purple curve is the spectrum obtained from samples containing magnetic particles in the absence of any applied magnetic field. When a magnetic field is applied, a peak in the light scattered intensity appears in the spectrum (red curve, Fig. 7). When the magnetic field is further increased, the position of the peak shifts towards smaller wavelengths. This is in agreement with the fact that the distance between the particle in chains decreases when the strength of the magnetic attraction increases. These observations confirm that the peak is due to the diffraction of light by the magnetic chains suspended in solution. This effect can be described quantitatively as follows: The light which is scattered by the suspension is proportional to the scattering cross-section $\mathrm{d}\sigma/\mathrm{d}\Omega$, for an incident wave vector $\mathbf{k}$ and an outgoing wave vector $\mathbf{k}'$. In the case of a monodisperse suspension of N identical particles which act as independent scatterers, this cross-section can be written as

$$\frac{\mathrm{d}\sigma}{\mathrm{d}\Omega} = NP(\mathbf{q})S(\mathbf{q}), \tag{14}$$

where $\mathbf{q} = \mathbf{k} - \mathbf{k}'$ is the momentum transfer of the light, $P(\mathbf{q})$ is the form factor, and $S(\mathbf{q})$ is the structure factor. The form factor depends on the shape of the particles but not on their concentration whereas the structure factor depends on the concentration and on the spatial organization of the particles. The structure factor is generally defined as [26]

$$S_N(\mathbf{q}) = \frac{1}{N}\sum_{i=1}^{N}\sum_{j=1}^{N}\langle e^{i\mathbf{q}\cdot(\mathbf{r}_i - \mathbf{r}_j)}\rangle, \tag{15}$$

where $\mathbf{r}_i$ are the positions of the scattering particles. In the geometry appropriate to the experiments discussed here, $q = |\mathbf{q}\cdot\mathbf{z}| = 2\pi n(1+\cos\theta)/\lambda$, where $\mathbf{z}$ is the axis of the chain, $n = n_w$ is the refractive index of the continuous phase (here water), λ is the wavelength of light in vacuum, and θ is defined in Figure 3. Since the variation of the form factor is smooth in the range of wave vectors used in the experiments, the peak which is observed in the scattered light at a specific wavelength can be attributed to the shape of the structure factor. When the magnetic field is turned on, the chain starts to form, and as a result a peak in the structure factor appears at a wave vector corresponding to the inverse of the lattice spacing of the chain. It is well known that no true long-range order exists in one-dimensional condensed systems (a consequence of the Mermin Wagner theorem [26]). It is less well known that this result only applies to systems of large size (*i.e.* in the thermodynamic limit). In the present situation, the system size is very small (typically 10 to 20 particles), so in this case the particle positions are not very different from what they would be if there were no thermal fluctuations. This can be justified by looking more precisely at the width of the Bragg peak, and comparing contributions to this width due to finite size effects and that due to thermal fluctuations. We give a simple estimate below that shows that for such small system sizes the contribution of thermal fluctuations is negligible, as we have also checked by studying more complicated models for the structure factor incorporating both effects. In view of this, we ignore below the fluctuations of the particles about their equilibrium position in the modeling of the structure factor, and we describe the chain as a perfect one dimensional lattice of particles with a spacing d, for which the structure factor is simply

$$S_N(\mathbf{q}) = \frac{1}{N}\left[\frac{\sin\left(N\frac{qd}{2}\right)}{\sin\left(\frac{qd}{2}\right)}\right]^2. \tag{16}$$

The maximum of the structure factor occurs when $qd = 2k\pi$, where $k = 1, 2, 3\ldots$, in agreement with Bragg's law.

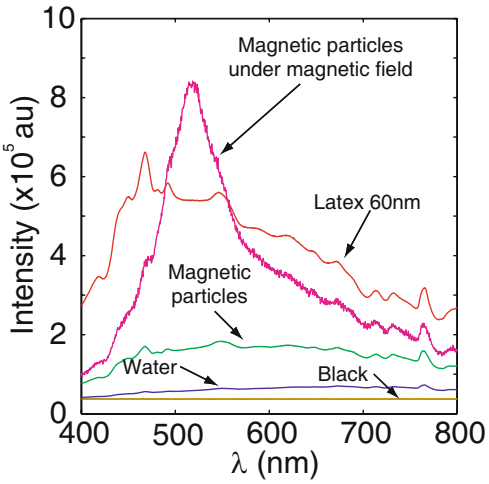

Fig. 8. (Colour online) Spectra of light scattered by water (blue curve), magnetic particles at $B = 0$ (green curve), particles of diameter 60 nm made of latex (red curve), magnetic particles under magnetic field (magenta curve) and without illumination (yellow curve).

In the vicinity of the first peak, equation (16) can be approximated by a Lorentzian

$$S_N(\mathbf{q}) = N\frac{\sigma^2}{\sigma^2 + 4(\tilde{q}d)^2} \tag{17}$$

with $\tilde{q} = q - 2\pi/d$ and

$$\left(\frac{\sigma}{2}\right)^2 = \frac{12}{N^2 - 1}\,. \tag{18}$$

The half-width of this Lorentzian at half-maximum is $\Delta\tilde{q} = \sigma/2d$, in other words the total width of the peak is σ/d. The contribution of thermal fluctuations to this quantity can be estimated by calculating the curvature of the potential of interaction near its minimum divided by k_BT, which leads to an estimate of the half-width due to thermal fluctuations $(\Delta\tilde{q})_{th}$. Even for the lowest magnetic field used in the experiment and with $N \simeq 10$–20, the ratio $(\Delta\tilde{q})_{th}/\Delta\tilde{q}$ is smaller than 10^{-3}, so particles are very well confined near their equilibrium position. This justifies the neglect of the thermal fluctuations in the analysis.

Our simplified form of the structure factor exhibits the following features: the height of the peak increases linearly with N while the width of the peak decreases as $1/N$ (assuming $N \gg 1$). Therefore it is possible to obtain an estimate of the average number of particles in the chains from the structure factor, which we do by measuring the width of the peak. This is a useful information, which we will later use to investigate the validity of the model developed by Zhang and Widom [23]. The spectra, obtained when a magnetic field is applied, exhibit a non-regular shape and are highly non-symmetrical. In addition to the contribution of the form factor and that of the structure factor, the response function of the detector and the spectrum of the light source must be taken into account to explain these spectra. Figure 8 shows the spectra obtained from different samples made of magnetic particles with and without applied field (green and magneta curves), of highly monodisperse and calibrated latex particles 60 nm in diameter, of pure deionized water (blue curve) and of a black sample obtained with no sample illumination (yellow curve). These signals are observed for samples with pure water only, with colloids of calibrated diameter of 60 nm and with magnetic colloids with and without applied magnetic field. The black sample shows that there is an offset I_{off} on the intensity measured by the detector. This offset is constant and does not depend on the wavelength. The signal obtained with a sample filled with pure water sample is slightly higher that that of the black, but the difference between both signals is very small. This phenomenon is due to the presence of a small amount of impurities, on the glass of the sample or in the water, which scatter the incident light beam in the direction of the detector. This signal I_{imp} is small as compared to the other signals, and may be removed if necessary by using a index matching bath. For the 60 nm particles (red curve), the spectrum has a "bell" shape. At high wavelength, the intensity decreases. This is a contribution of the form factor. The result is in agreement with Rayleigh's law, that is, the scattered intensity decreases as $\frac{1}{\lambda^4}$, where λ is the wavelength. Interestingly, at small wavelengths, the intensity decreases when the wavelength decreases. This decrease is due to the response function of the camera whose quantum yield is not uniform over the whole spectrum, and decreases at small wavelength. The instrument response function R_f, which includes both the light source and the detector must be taken into account as it affects the shape of the diffraction peak. As explained below, the signal can be processed in order to remove the response function of the detector and the contribution of the light source, to determine accurately the structure factor.

We will denote $I(\lambda, B_e)$ as the signal measured on the detector with a magnetic field B_e, and express all quantities of interest in terms of the wavelength λ rather than as done previously in terms of q. The signal measured on the detector can be approximated by

$$I(\lambda, B_e) = I_{off} + (NP(\lambda)S(\lambda, B_e) + I_{imp}(\lambda))R_f(\lambda), \tag{19}$$

where N is the number of scattering particles, $P(\lambda)$ is the form factor of the particles and $I_{imp}(\lambda)$ the light intensity scattered by impurities, which may be located on the glass walls of the sample. $S(\lambda, B_e)$ is the structure factor of the chains. When no magnetic field is applied, there is no chain suspended in solution: $S(\lambda, B_e = 0) = 1$. If we assume that $I_{imp}(\lambda)$ is small compared to the other signals, we have

$$S(\lambda) \simeq \frac{I(B_e \neq 0) - I_{off}}{I(B_e = 0) - I_{off}}\,. \tag{20}$$

The estimated structure factor obtained after processing the measured signals in this way is represented in Figure 9 for different values of the magnetic field. We found that the position of the peak before and after the treatment is displaced by less than 4 nm. If the scattered intensity is not processed in this way, an error in the interparticle distance measurement of $\sim$ 1 nm is propagated.

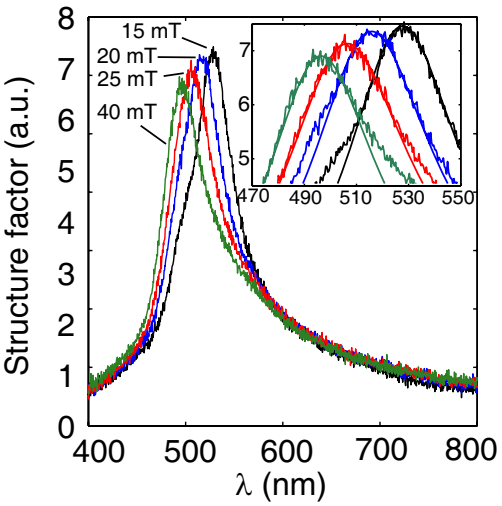

Fig. 9. (Colour online) Structure factors obtained for different intensities of magnetic field, 15 mT (black), 20 mT (blue), 25 mT (red) and 40 mT (green). Inset: The peaks of the curves are well fitted by a Lorentzian (Eq. (17)). The width of the Lorentzian gives an estimate of the number of particles in the chains (from right to left: 15 mT (black), 20 mT (blue), 25 mT (red) and 40 mT (green)).

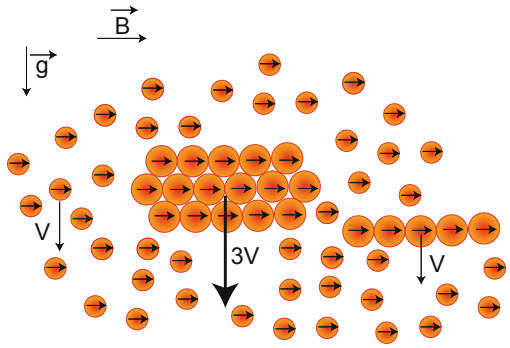

Fig. 10. Particles sorting principle leading to a monodisperse solution of particles. Single particles and a chain of particles have approximately the same sedimentation velocities. Bundles of particles sedimentate much faster as their velocity is proportional to the thickness of a bundle. The magnetic fractionated method is based on this phenomenon.

However, if the backscattering signal is very strong, the position of the peak can be directly estimated from the raw data.

In order to get an estimate of the number of particles in the chain, the structure factor is fitted by the Lorentzian given in equation (17). Any small impurity or dust in our system has a strong influence on the height of the peak. Therefore the height is not used to extract the length of the chains. However, the width of the peak does not depend on such factors, which is why we used the width of the best fitting Lorentzian to determine the average number of particles in the chains. We find that the number of particles in the chains must be $N = 10 \pm 1$ particles per chain, to fit the curves (inset Fig. 9). This number was also determined directly by video-microscopy. Since the particles are very small, the microscopy measurements are only approximative but provide an estimate of the average sizes of the chains of around 14 particles. We have thus a good agreement with the length extracted from the structure factor.

3.3 Superparamagnetic colloid characterization

In the early use of the MCT, magnetic emulsion had to be specially prepared for the purpose of the experiment: it was a limiting factor for wider acceptance of the method. Now, the particles are commercially available from Ademtech (`www.ademtech.com`). They are also produced using a ferrofluid emulsion to insure a very high magnetic content, and are coated with polymers for further macromolecules grafting [27,28]. We describe in this part how to prepare the commercial batch from Ademtech in order to perform MCT measurements. We then characterize their magnetic properties, so we can compute the magnetic force from the distance measurements. We also characterize their optical properties, in order to check the Bragg's law validity in the following section.

3.3.1 Mean size and monodispersity

As stated, our technique is based on the diffraction by a chain of particles. The diffraction peak is strong and well defined if particles are very monodisperse. In addition monodispersity suppresses strong hysteresis effects during chain formation. Indeed within a suspension of polydisperse particles, one can observe that upon slowly increasing the magnetic field, large particles chain first and small particles aggregate on the side of these chains. In contrast, if the field is suddenly applied, all particles, large and small are located randomly inside each chain. It is therefore necessary to use monodisperse suspensions to avoid this kind of side effect. Magnetic particles are commercially available from the Ademtech company with a polydispersity of around 20%. A magnetic fractionation method is used to reduce the polydispersity as much as possible. This method is based on the growth mechanism of magnetic chains in solution. Particles suspended in solution are isolated when no magnetic field is applied. When the magnetic field is applied, particles attract each other and form chains. For a well chosen magnetic field, large particles will form chains, whereas smaller ones will remain unaggregated. If particles are concentrated enough ($\phi_v = 1\%$), and if the salt concentration is high enough to screen electrostatic interactions ([NaCl] = 50 mM), chains interact and form bundles [29] as shown schematically in Figure 10. The magnetic fractionated method is based on the fact that single particles, chains and bundles have different sedimentation velocities.

More precisely, the sedimentation velocity of a singlet is given by the balance between the frictional resistance due to viscous drag $F_v = 6\pi\eta a V_{sed}$, where η is the viscosity of the solution and V_{sed} is the sedimentation velocity, and the buoyancy force $F_b = \frac{4}{3}\pi a^3 \Delta\rho g$, where g is

the gravity constant and $\Delta\rho$ is the density difference between the particle and the fluid. This balance leads to the following expression for the single particle sedimentation velocity:

$$V_{sed} = \frac{2}{9}\frac{\Delta\rho g}{\eta}a^2\,. \tag{21}$$

For a chain of N particles, the viscous friction force is $F_v = 4\pi\eta(2Na)V_{sed}$ [30] and the buoyancy force is $F_b = N\frac{4}{3}\pi a^3\Delta\rho g$. Therefore the number of particles N cancels out, and the sedimentation velocity is

$$V_{sed} = \frac{1}{6}\frac{\Delta\rho g}{\eta}a^2\,, \tag{22}$$

which is of the same order of magnitude as the sedimentation velocity of a singlet: with sedimentation it is not possible to separate a single particle from a chain, whatever its length. Now consider a bundle of N' chains of N particles (Fig. 10). For a bundle, the length of the chains N is large compared to its width N'. For a slender body which moves in the low Reynolds number, the characteristic length is the longest length $2Na$ [30]. Therefore, the viscous friction force remains $F_v = 4\pi\eta(2Na)V_{sed}$ [30], but the buoyancy force is now $F_b = N'N\frac{4}{3}\pi a^3\Delta\rho g$. Therefore the sedimentation velocity of a bundle is

$$V_{sed} = N'\frac{1}{6}\frac{\Delta\rho g}{\eta}a^2\,, \tag{23}$$

which shows that a bundle has a very fast sedimentation velocity as compared to a single chain or a single beads. Sedimentation can therefore be used to separate particles from bundles of chains. When a magnetic field is applied, one can assume that particles form a chain when their interaction energy is higher than the thermal energy k_BT. The dimensionless number Λ defined by

$$\Lambda = \frac{-U_{mag}}{k_BT} = \frac{\frac{\pi}{18\mu_0}a^3B^2}{k_BT} \tag{24}$$

compares these two energies, where B is the local magnetic field, μ_0 the magnetic permeability, a the radius of the bead, k_B Boltzman's constant and T the temperature. For $\Lambda > 1$, the magnetic energy dominates the thermal energy, so the chain aggregation process occurs while the magnetic field is applied. For $\Lambda < 1$, thermal fluctuations prevent the formation of chains. At constant magnetic field, particles whose radius a is such that $a < (\frac{k_BT}{\frac{\pi}{18\mu_0}B^2})^{\frac{1}{3}}$ remain isolated in solution and sediment slowly. Particles of radius a such that $a > (\frac{k_BT}{\frac{\pi}{18\mu_0}B^2})^{\frac{1}{3}}$ form bundles and sediment quickly. This is the basis of the magnetic fractionated method.

A solution of polydisperse particles at a concentration $\phi_v = 1\%$ suspended in a MES buffer with 50 mM added sodium chloride was subjected to a homogeneous horizontal magnetic field. After 60 min, two phases were obtained, a concentrated one at the bottom of the sample, containing mainly big particles, and a very dilute one containing small particles. The two phases were extracted by pipetting, their concentration measured by turbidimetry is adjusted again to $\phi_v = 1\%$, and the experiment is iterated four times. The particle distribution is measured using a disk centrifuge (CPS instrument). The improvement in the monodispersity is shown in Figure 11. With such a method polydispersity is reduced from $\approx 20\%$ to $\approx 7\%$.

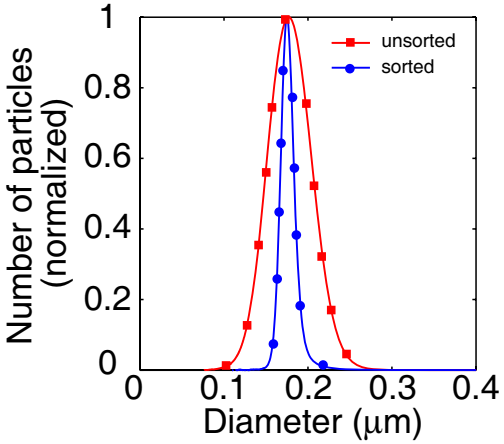

Fig. 11. Particles polydispersity before and after the sorting. The magnetic fractionated method allows us to greatly improve the particles polydispersity.

3.3.2 Magnetic properties

Following the suspension fractionation, the magnetic and optical properties of the monodisperse colloids can be investigated. The magnetic and optical properties mainly depend on the size of the particles, and their iron oxide content. In order to measure Fe content, the particle size, volume and mass fraction are measured. The mean radius of the particles is measured accurately by light scattering with a CGS3 apparatus (ALV GmbH) with a laser beam of wavelength $\lambda = 632.8$ nm. The mean radius a is found to be equal to $a = 90.0 \pm 0.9$ nm. The radius usually measured by light scattering is the so-called hydrodynamic radius. In our case, the particles are stabilized with a surfactant that is so small that we can reasonably assume that it does not contribute to the hydrodynamics radius. Once the particles of known radius are inserted in the centrifuge, the density of the particles themselves is estimated to $\rho_p = 2.04 \pm 0.04\,\mathrm{g/cm^3}$. The density of the solution of particles was measured with a densitometer, $d_{sb} = 0.998912 \pm 0.000004$, which gives rise to a volume fraction of $\phi_v = (6.02 \pm 0.2)\cdot 10^{-2}\%$ and a mass fraction of $\phi_m = (1.23 \pm 0.06)\cdot 10^{-1}\%$. The magnetic properties are shown in Figure 12. They were studied by using a squid magnetometer, as described in reference [31]. To measure a colloidal force-distance profile, magnetic fields of variable intensities are applied. It is therefore very important to take into account the fact that the magnetic susceptibility of the particles strongly depends on the applied magnetic field.

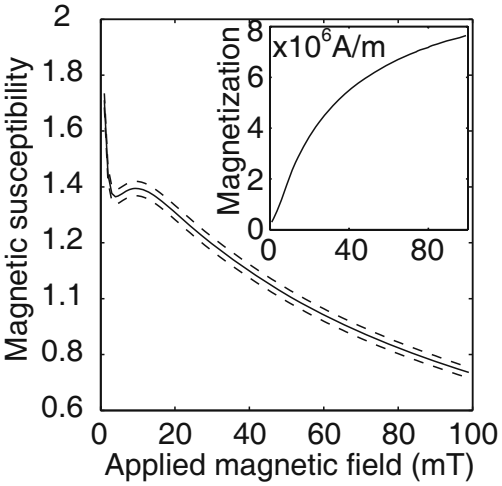

Fig. 12. Magnetic susceptibility as a function of the applied external magnetic field. The inset shows the magnetization as a function of the external applied magnetic field. Results adapted from [31].

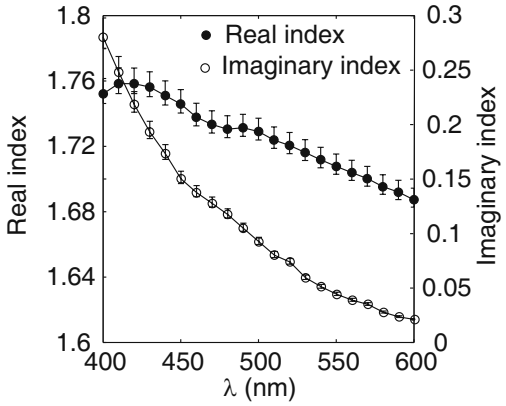

Fig. 13. Real refractive index (full circles) and imaginary refractive index (empty circles) as a function of wavelength. The real index does not depend on the wavelength, while the imaginary index has a strong dependence on the wavelength.

3.3.3 Optical properties

The optical real and imaginary indices of the particles and their dependence on wavelength are measured using an integration sphere by a method analogous to that of Ma *et al.* [32]. The results are presented in Figure 13. They exhibit a very small dependence of the real index on the wavelength. In contrast, the imaginary index has a strong dependence on the wavelength. This is due to inclusions of iron oxide, which is known to absorb light at low wavelength.

4 Performance of the technique

4.1 Bragg's law assumption

The distance d between the particles is derived from the analysis of the signal diffracted by the chains. Leal Calderon *et al.* [8] directly applied Bragg's law in order to measure d. However Bragg's law assumes that the light is scattered only once by each scatterer, which means that the incident light on all particles is the same. It neglects coherent scattering effects which occurs when light is scattered more than once by a given scatterer. This effect becomes important when particles are very close, as in our case. We further use the same type of approximation to separate the scattered signal into a form factor and a structure factor. To check the validity of Bragg's law, we perform simulations using Mackowski's algorithm [33] available at the url: `http://www.giss.nasa.gov/~crmim/t_matrix.html`. Mackovski's algorithm performs a rigorous calculation of the diffracted light scattered by a chain of particles. It is based on the calculation of so called T-matrix, which leads to a general solution of Maxwell equations in the case of a distribution of scatterers. The simulation is run under the assumption that the radius of the particles is $a = 90\,\text{nm}$, the interparticle distance is $d = 190\,\text{nm}$, the index of the water is $n = 1.33$ and the indices of the particles are those taken from previous section. Bragg's law predicts the diffracted wavelength to be $\lambda = 505.4\,\text{nm}$, whereas the simulation gives $\lambda = 512\,\text{nm}$ for a chain of 10 beads. The diffracted wavelength depends slightly on the length of the chains, but in all cases it is only around 1% higher than the prediction deduced from Bragg's law. The maximum amplitude of the computed structure factor for a chain of N particles is also higher than N, the value given by equation (16) based on Bragg approximation. Accordingly, the peak width is slightly underestimated using equation (17). These effects can be understood as originating from the fact that scattering amplitude from each particle in the chain is different from the scattered amplitude from a single particle: the separation of the scattered intensity in form factor and structure factor (Eq. (14)) does not hold. If we increase the interparticles distance, simulations converge to Bragg's law predictions. Therefore, for the sake of simplicity, Bragg's law is used to derive the distance between the particles: this assumption leads to an absolute error on the distance of about 1% maximum.

4.2 Magnetic force: finite-size effect

In the calculation of the magnetic force from the distance measurement, we have to take into account the long-range character of the magnetic force: all neighbors within the chain contribute to the force. For simplicity, we have assumed, as discussed by Zhang and Widom [23], that the chain is of infinite length. As a consequence, the interparticle distance d, the magnetization m and the forces are constant within the chain. In real experiments, video microscopy images with the same volume fraction of beads show that chains length is about 10 to 20 beads. With a real chain, the magnetization and the force are smaller at the ends of the chain. In order to test the validity of the infinite chain approximation, we have performed some numerical simulations. We computed the

Table 1. Relative error on magnetization m, force F and distance d for particles at one chain end as compared to an infinite chain. Beads are numbered from one end, so bead no. 1 is at one end.

Bead number	1	2	3
$\Delta m/m$ (%)	10.2	2.6	1
$\Delta F/F$ (%)	20.8	6.6	2.6
$\Delta d/d$ (%)	1.2	0.3	0.1

equilibrium positions of N beads in a chain, submitted to the magnetic force and an electrostatic repulsion. We used the expression (13) for the electrostatic force, with beads surface potential of -35 mV, and an ionic strengths 1 mM corresponding to a Debye length of 9.61 nm. The magnetic force exerted by particle i on particle j is

$$\mathbf{F}_{j\to i} = \frac{3\mu_0 m_i m_j}{2\pi d_{ij}^4}\mathbf{e}_r\,, \tag{25}$$

where d_{ij} is the distance between the two particles, and m_i the dipolar moment of particles i. This dipolar moment m_i is related by equation (8) to the local field $\mathbf{B}_i$ at the location of particle i by

$$\mathbf{B}_i = \mathbf{B}_e + \sum_{j\neq i}\mathbf{B}_{dip}^{j\to i} = \mathbf{B}_e + \sum_{j\neq i}\frac{\mu_0 m_i m_j}{\pi d_{ij}^3}\mathbf{e}_r\,. \tag{26}$$

The mechanical equilibrium is obtained numerically by iteration, for $\Lambda = 100$, where Λ is the number which compares the magnetic energy with the thermal energy (see expression (24)). As expected, we observe a deviation from the infinite chain model only at the ends of the chain: the magnetic moment and the force are smaller on the edges than in the center of a long chain, so interparticle distances are slightly bigger in the ends. Typical values are given in Table 1. Since the electrostatic (or steric) forces decay exponentially with the distance, the error on the distance is far less important than on the force.

In order to test the role of the edges on the structure factor, we performed simulations for chains from 2 to 50 beads. From the position of the beads, we compute the structure factor using equation (15), with the approximation of independent scatters. There is a clear shift towards smaller wavelength with increasing chains length (Fig. 14). Using chains with 10 particles or more limits the error on λ to less than 2 nm.

We indeed observe experimentally at short time, after switching on the magnetic field, a clear shift towards smaller wavelength of the peak, reflecting the chains formation. Moreover, we also observe that the height of the peak increases, and its width decreases with time, as can be predicted from the expression of the structure factor (Eq. (16)) for a growing chain. With a bead volume fraction $\phi_v = 0.003\%$, we waited for 60 s before measuring the beads position, so the chain are approximately 10 beads long, as discussed in Section 3.2. Our setup allows us to use even more dilute samples, but finite size effects will become significant under these conditions. A solution is to decrease the sample thickness, keeping the volume fraction constant. We have checked that a 10 μm cell, with $\phi_v = 0.003\%$, is sufficient to perform measurements.

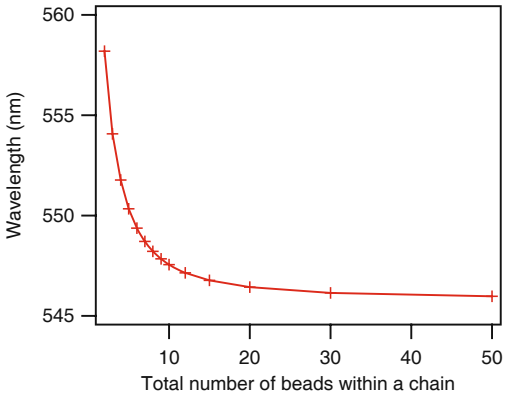

Fig. 14. Simulations giving the position of the maximum of the structure factor as a function of the number of particles in a chain. Magnetization and magnetic force are smaller at chain ends, so the average interparticle distance is larger for a short chain. As the number of particles increased, the two ends influence is less pronounced, and we recover the infinite chain approximation value.

4.3 Error estimates

The absolute accuracy of the particle separation distance is altered for two different reasons: the first reason is due to the difference in the diffraction peak position between Bragg's law and the exact solution of diffraction by a lattice of spheres. The distance between the colloids is derived using Bragg's law, but there exists a shift between Bragg's prediction and Mackowsky's simulation of around 2 nm. The second source of error is related to the permanent evolution with time of the measurement. At short time, typically 1 or 2 mins after applying the magnetic field, there is a clear shift towards smaller wavelength of the peak, associated with a significant increase of the peak height. We attribute this behavior to the increase of chains length with time, as detailed previously. At longer time, there is still a small residual drift towards smaller wavelength of the peak, associated in that case with a decrease of the peak height. This long time behavior is more pronounced for weak interparticle interactions, so we attribute this behavior to the lateral thickening of the magnetic chains [29]. Somewhat arbitrarily, the measurements of the distance between the particles is performed when the amplitude of the signal is maximal. This gives rise to an uncertainty of the distance of around 2 nm. This technique has an accuracy for the distance between the magnetic colloids of 4 nm, which corresponds to a subsequent accuracy for the force of 0.8 pN.

The resolution of this technique is estimated by measuring the position of the diffraction peak in the same conditions. The variability of the measurements is around 1 nm, which corresponds well to the shifts observed between the experimental points and the fitting curves in

Figure 5. From these errors, the resolution on the force measurement is around 0.2 pN, which corresponds to a surface energy resolution of $7 \cdot 10^{-7}\,\mathrm{J\,m^{-2}}$. Though this technique is not ideally suited to the measurement of absolute distance, as is the case for other techniques such as OT or AFM, the magnetic chaining technique shows an excellent resolution in term of distance and force analogous to that of the atomic-force microscopy.

5 Conclusion

We have presented the theoretical and experimental aspects of the magnetic chaining technique. The step-by-step methodology used for characterizing the properties of the magnetic colloids (size, refractive index, monodispersity, magnetic susceptibility) has been described as well as the performance estimates for this technique in terms of force and distance accuracies. This technique appears to be easy to use and offers the possibility of measuring any kind of repulsive forces between magnetic colloids with excellent accuracy. Moreover, our new experimental setup allows us to perform measurements on samples of very small volume, which makes this technique very useful for studying biological molecules or processes [15,18].

This work was supported by the French Ministry of Research. The authors acknowledge Anne Koenig, Emanuel Bertrand, Cécile Goubault, Fernando Leal-Calderon, Laetitia Cohen-Tannoudji for fruitful discussions, and Andrew Hollingsworth for his careful reading of this manuscript.

References

1. D.C. Prieve, Adv. Colloid Interface Sci. **82**, 93 (1999).
2. D. Leckband, J. Israelachvili, Q. Rev. Biophys. **2**, 105 (2001).
3. G. Binnig, C.F. Quate, C. Gerber, Phys. Rev. Lett. **56**, 930 (1986).
4. V. Bergeron, C. Radke, Langmuir **29**, 3020 (1992).
5. J.C. Crocker, D.G. Grier, Phys. Rev. Lett. **73**, 352 (1994).
6. J.C. Crocker, D.G. Grier, J. Colloid Interface Sci. **179**, 298 (1996).
7. F.H.C. Crick, A.F.W. Hughes, Exp. Cell. Res. **1**, 37 (1950).
8. F. Leal Calderon, T. Stora, O. Mondain-Moncal, P. Poulin, J. Bibette, Phys. Rev. Lett. **72**, 2959 (1994).
9. J. Philip, O. MondainMonval, F. Leal-Calderon, J. Bibette, J. Phys. D **30**, 2798 (1997).
10. O. Mondain-Monval, A. Espert, P. Omarjee, J. Bibette, F. Leal-Calderon, J. Philip, J.F. Joanny, Phys. Rev. Lett. **80**, 1778 (1998).
11. J. Philip, O. Mondain-Monval, F. Leal-Calderon, J. Bibette, Bull. Mater. Sci. **22**, 313 (1999).
12. J. Philip, T. Jaykumar, P. Kalyanasundaram, B. Raj, O. Mondain-Monval, Phys. Rev. E **66**, 011406 (2002).
13. J. Philip, G.G. Prakash, T. Jaykumar, P. Kalyanasundaram, O. Mondain-Monval, B. Raj, Langmuir **18**, 4265 (2002).
14. J. Philip, G.G. Prakash, T. Jaykumar, P. Kalyanasundaram, B. Raj, Phys. Rev. Lett. **89**, 268301 (2002).
15. A. Koenig, P. Hebraud, C. Gosse, R. Dreyfus, J. Baudry, E. Bertrand, J. Bibette, Phys. Rev. Lett. **95**, 128301 (2005).
16. F. Montagne, S. Braconnot, A. Elaissari, C. Pichot, J.C. Daniel, B. Mandrand, O. Mondain-Monval, J. Nanosci. Nanotechnol. **6**, 2312 (2006).
17. T.D. Dimitrova, F. Leal-Calderon, Langmuir **15**, 8813 (1999).
18. C. Goubault, P. Jop, M. Fermigier, J. Baudry, E. Bertrand, J. Bibette, Phys. Rev. Lett. **91**, 260802 (2003).
19. J. Baudry, E. Bertrand, C. Rouzeau, O. Greffier, A. Koenig, R. Dreyfus, L. Cohen-Tannoudji, C. Goubault, L. Bressy, L. Vincent, N. Lequeux, J. Bibette, Ann. Chim. - Sci. Mater. **29**, 97 (2004).
20. R. Dreyfus, J. Baudry, M. Roper, M. Fermigier, H.A. Stone, J. Bibette, Nature **437**, 862 (2005).
21. O. Mondain-Monval, F. Leal-Calderon, J. Philip, J. Bibette, Phys. Rev. Lett. **75**, 3364 (1995).
22. J. Bibette, J. Magn. & Magn. Mater. **122**, 37 (1993).
23. H. Zhang, M. Widom, Phys. Rev. E **51**, 2099 (1995).
24. J. Israelachvili, *Intermolecular and Surface Forces*, 2nd edition (Academic Press, 2003).
25. C. Gutsche, U.F. Keyser, K. Kegler, F. Kremer, Phys. Rev. E **76**, 031403 (2007).
26. P.M. Chaikin, T. Lubensky, *Principles of Condensed Matter Physics* (Cambridge University Press, 1995).
27. F. Montagne, O. Mondain-Monval, C. Pichot, H. Mozzanega, A. Elaissari, J. Dispers. Sci. Technol. **24**, 821 (2003).
28. F. Montagne, S. Braconnot, O. Mondain-Monval, C. Pichot, A. Elaissari, J. Magn. & Magn. Mater. **250**, 302 (2002).
29. E.M. Furst, A.P. Gast, Phys. Rev. E **62**, 6916 (2000).
30. K. Zahn, R. Lenke, G. Maret, J. Phys. II **4**, 555 (1994).
31. P.C. Fannin, L. Cohen-Tannoudji, E. Bertrand, A.T. Giannitsis, C. Mac Oireachtaigh, J. Bibette, J. Magn. & Magn. Mater. **303**, 147 (2006).
32. X.Y. Ma, J.Q. Lu, R.S. Brock, K.M. Jacobs, P. Yang, X.H. Hu, Phys. Med. Biol. **48**, 4165 (2003).
33. D.W. Mackowsky, J. Opt. Soc. A **13**, 2266 (1996).